Applied Catalysis B: Environmental 129 (2013) 163–171

Contents lists available at SciVerse ScienceDirect

Applied Catalysis B: Environmental

journal homepage: www.elsevier.com/locate/apcatb

The graphene-supported palladium and palladium–yttrium nanoparticles for the oxygen reduction and ethanol oxidation reactions: Experimental measurement and computational validation

Min Ho Seo [a], Sung Mook Choi [b], Joon Kyo Seo [a], Seung Hyo Noh [a], Won Bae Kim [b,*], Byungchan Han [a,**]

[a] Department of Energy Systems Engineering, Daegu Gyeongbuk Institute of Science and Technology (DGIST), Daegu 711-873, South Korea
[b] School of Materials Science and Engineering, Gwangju Institute of Science and Technology (GIST), Gwangju 500-712, South Korea

ARTICLE INFO

Article history:
Received 26 May 2012
Received in revised form 30 July 2012
Accepted 7 September 2012
Available online 15 September 2012

Keywords:
Electrocatalyst
Graphene
Palladium
Oxygen reduction reaction
Ethanol oxidation reaction
Alkaline fuel cell
Density functional theory

ABSTRACT

Oxygen reduction and ethanol oxidation reaction (ORR and EOR) have been studied on graphene nanosheet-supported (GNS) pure Pd and Pd_3Y nanoscale-alloy (Pd/GNS and Pd_3Y/GNS) electrocatalysts. The electrochemical studies were carried out for ORR both in acidic and alkaline solutions employing a rotating disk electrode (RDE), and performed for EOR in alkaline media with cyclic voltammetry method. The structure and composition of the Pd and Pd_3Y nanoparticles were verified using TEM, XRD and XPS. We combine the experimental measurements with *ab initio* density functional theory (DFT) calculations to identify the d-band center position of Pd atom in the pure Pd and Pd_3Y alloys as a function of site on near the surface. Both approaches clearly show that alloying the Pd with Y significantly modifies the electronic structures of Pd atoms. Core-level of Pd $3d_{5/2}$ shifts to a negative value, which increases the d-band center of Pd atom and enhances the bond strength of Pd—O, which implies good catalysts for EOR but ORR. Our results indicate that the electronic structure of the Y-modified bimetallic Pd alloy is a good descriptor for the catalytic activity.

1. Introduction

Acid-based polymer electrolyte fuel cells (PEMFCs) are now accepted as clean and efficient energy generation systems at low temperatures (<100 °C) [1]. For PEMFCs to be a realistic option, however, the problems of the high materials cost and the low efficiency of the Pt-based electrode catalysts must be solved. Several approaches have attempted not only to decrease the amount of Pt loading [2–6], but also replace it with cheaper materials while maintaining high ORR activity [7–10]. Recently, with the development of anion exchange membrane (AEM), alkaline fuel cells (AFCs) got lots of attention due to utilizing other metal such as Pd and Ag instead of conventional Pt catalysts [11–13]. Pd is approximately five times cheaper than Pt but is also more electrochemically stable in acidic (or alkaline) electrolyte compared with other catalytic metals, such as Fe, Co, Ni and Cu [1,14–16]. The Pd-based catalysts have demonstrated to be active for ORR as much as the state of the art carbon-supported Pt under acidic conditions [17–20]. In the previous report, we showed that Pd nanoparticles on GNS are more favorable ORR catalysts than the Pt nanoparticle even in alkaline condition [7]. In addition, Pd catalyst, notably, has known to be more effective than the Pt catalysts for the electrooxidation of alcohol, such as ethanol and methanol [7,21–24] under alkaline conditions.

However, the catalytic performances of Pt and Pd are not still enough for practical applications [25–27]. Alloying with other metals to improve the catalytic activities of Pt and Pd for several fuels could be improved through the alloying with 2nd and 3rd metal [17–20,27]. The mechanistic details of the catalysis for ORR and EOR, however, were not yet fully understood. The correlation between electronic structure and alloying may be the clue to understanding catalytic behavior. It is difficult to experimentally obtain the direct information of the electronic structures of the alloy catalysts in valence level. For example, the application of conventional X-ray photoelectron spectroscopy (XPS) might lead to serious misinterpretation due to contaminations from the atmosphere [28,29]. On the other hand, *ab initio* density functional theory (DFT) computational methods have been proved an accurate to provide information of electronic structures

* Corresponding author. Tel.: +82 62 715 2317; fax: +82 62 715 2304.
** Corresponding author. Tel.: +82 53 785 6412; fax: +82 53 785 6409.
E-mail addresses: wbkim@gist.ac.kr (W.B. Kim), hanbc@dgist.ac.kr (B. Han).

0926-3373/$ – see front matter © 2012 Elsevier B.V. All rights reserved.
http://dx.doi.org/10.1016/j.apcatb.2012.09.005

of heterogeneous alloy catalysts [25–27]. The d-band center model proposed by Nørskov and associates was turned out to be very useful for describing the underlying mechanisms of experimentally observed complicated surface catalytic reactions [18,27,30–34]. The model stands on the assumption that the weighted average of d-band electrons energies (d-band center) of a catalyst is strongly correlated with binding energy of the catalyst atoms with the chemical species adsorbed (e.g., oxygen) [14,30,32,34], that is, the closer the position of the d-band toward the Fermi level the stronger interactions [18,27,32–34]. Based on their model, the d-band center of Pt seems too high to be an efficient ORR catalyst [27,32–34]. It was proposed that the electronic structure of d-band center should be modified by several methods, such as alloying with other metals or changing their alloying compositions, varying particles size and so on [18,27,32–34]. For example, Pt_3Ni alloy shifts the d-band center of Pt downward, and indeed shows faster kinetics than pure Pt [35]. Like Pt, Pd also shows a strong interaction with oxygen, implying low efficiency for the ORR [18]. Therefore, it is necessary to control the d-band center position of Pd through alloying with second metals. Likewise, the Pd_3X alloys (X = Y, Cd, Zn, Ni, Co, etc.) with weaker oxygen binding than conventional Pt also have been predicted for the ORR activities by DFT calculation [18,27,32–34]. In addition, the bimetallic catalysts may have higher efficiency for electrooxidation of ethanol as well [25,26].

For the high functional performance, metal alloy catalysts should be deposited on support materials of specific properties, such as a large surface area to provide high metal dispersion, a suitable porosity to boost gas flow, a high electrical conductivity to facilitate electron transfer, and a high stability under the electrochemical conditions of fuel cells [36]. Graphene nanosheets (GNS) have excellent physicochemical properties, such as a large surface area (theoretically, ca. 2630 $m^2\,g^{-1}$) [37], chiral quantum hall effects [38,39], high thermal and electronic conductivity [40], and high mechanical strength [41]. GNS, in particular, has a high specific surface area compared with the commercial amorphous carbon (about 300 $m^2\,g^{-1}$). Recently, experimental or theoretical studies on metal-supported GNS catalysts showed that metal could be loaded up to 80 wt.% [3,7,42,43].

The purpose of this work is to identify the correlations between the catalytic activity of Pd and Pd alloy catalysts for ORR and EOR under acidic and alkaline media with the d-band center of Pd atoms. It is because the precise understanding of the mechanisms for the ORR is necessary to develop highly efficient catalysts. For this goal, GNS was employed for the deposition of Pd and Pd_3Y metal nanoparticles at loadings up to 60 wt.%. The GNS-supported Pd_3Y catalyst (Pd_3Y/GNS) is prepared by the impregnation of Pd and Y precursors on the GNSs without the use of a surfactant. X-ray diffraction (XRD), transmission electron microscopy (TEM), and X-ray photoelectron spectroscopy (XPS) analyses are performed to investigate the physicochemical properties of the prepared materials, such as particle size, and distribution, crystallinity and electronic properties. We extensively utilized *ab initio* DFT computations to locate the d-band center positions of the Pd atoms on pure Pd and Pd_3Y alloy with varying the atomic arrangement in the vicinity of surfaces, which is of importance to design the optimization of structure of Pd (1 1 1) and Pd_3Y (1 1 1) structures. The ORR performance of GNS-supported Pd_3Y catalysts of a high particle dispersion was investigated both in acidic and alkaline solutions through the use of a rotating disk electrode (RDE). Furthermore, the catalytic activities of the Pd/GNS and Pd_3Y/GNS catalysts for the ethanol electrooxidation reactions were examined using cyclic voltammetry technique. Our results show that experimental measurements and theoretical calculations on the electronic structures of Pd by alloying Y are well agreed, and d-band center of Pd is a good descriptor for the catalytic activities of Pd alloys.

2. Experimental

2.1. Preparation of GNS, and GNS-supported Pd and Pd_3Y nanoparticles

GNS was prepared according to the method reported in the literature [7,43,44]. GNS supports were synthesized with functionalization by surface epoxy, hydroxyl and carboxyl groups through simple synthetic processes. These processes include the chemical oxidation of common graphite-to-graphite oxide and the subsequent thermal exfoliation of the graphite oxide to GNS. GNS-supported metal nanoparticles were synthesized through the impregnation method combined with a heat treatment under hydrogen gas [3,6]. The palladium (II) nitrate ($Pd(NO_3)_2{\cdot}nH_2O$, KOJIMA Chemicals) salt was mixed with the yttrium(III) nitrate hexahydrate ($Y(NO_3)_3{\cdot}6H_2O$, Aldrich) salt. And then, the salts were added into the GNS dispersed in acetone. It was stirred using an ultrasonicator with a voltex mixer. The atomic ratio of Pd and Y element is 3:1 (Pd_3Y). The resulting slurry was dried in a convection oven at 100 °C for 10 h, which allowed acetone to evaporate. The mixture was then treated with 4% H_2 in N_2 gas at 250 °C for 3 h.

2.2. Physicochemical analyses of GNS-supported Pd_3Y nanoparticles

The transmission electron microscope (TEM, JEOL JEM-2100) was operated at 200 kV. All TEM samples were prepared by scraping the catalyst from the glassy carbon onto a Cu grid, onto which 6 μl of DI water was added dropwise. Drops of the DI water helped disperse the catalysts over the standard Cu grid (200 mesh). The Cu grid was then covered with a carbon film and dried for 1 h to allow the water to evaporate, which left the catalyst dispersed on the grid prior to being placed under the microscope.

The crystalline characteristics of the catalysts were examined by powder X-ray diffraction using a Rigaku Rotalflex (RU-200B) X-ray diffractometer equipped with a Cu Ka (l = 1.5405 Å) source and a Ni filter, which allowed us to characterize the structural evolution of the Pd crystallites in the catalysts. The source was operated at 10 kV and 10 mA, and the 2θ angular region between 30° and 90° was scanned at a rate of 1° min^{-1}.

For the Pd/GNS and Pd_3Y/GNS catalysts, the chemical states and surface compositions of the aforementioned samples were analyzed by X-ray photoelectron spectroscopy (XPS, ESCALAB 250, UK) with a monochromic Al Kα X-ray source (E = 1486.6 eV). No significant charging effects were detected. Data processing was performed with the XPSPEAK software program. The background was corrected using the Shirley method, and the binding energy (BE) of a C 1s peak from the support at 284.5 eV was used as an internal standard.

2.3. Computation details

We utilized *ab initio* DFT [45,46] calculations implemented in Vienna *ab initio* simulation package (VASP) program [47]. A slab model consisting of a 2 × 2 surface unit cell and nine close-packed layers in the direction of Pd (1 1 1) surface were employed to calculate the surface segregation energy of a Y atom in the Pd slab. A vacuum thickness of 18.03 Å was inserted around the slab, and a periodic boundary condition was imposed to the unit of slab + vacuum. The atoms in the top five layers were fully relaxed, while the atoms of the bottom four layers were fixed to their bulk positions. Moreover, model systems of a six layer slab stacked in the (1 1 1) direction of an FCC metal were designed to simulate Pd (1 1 1), Pd_3Y (1 1 1) and Pd_3Y^* (1 1 1) surfaces of 2 × 2 surface unit cell. The Pd_3Y^* (1 1 1) corresponding to Pd:Y atomic ratio of 3:1 denotes the Pd–Y alloy having with 50% Y in the 2nd layer from

the surface. We imposed the vacuum region of 12.25 Å to preclude interactions between the slab and its images. The atoms in the top three layers were fully relaxed, while the atoms of the bottom three layers were fixed to their bulk positions. To obtain total energies, first principles computations were performed with the projector augmented wave (PAW) method describing interactions between ions and electrons [48,49] and generalized gradient approximation (GGA) [47,50] to DFT by Perdew–Burke–Ernzerhof as implemented in VASP [50]. The cutoff energy for a plane wave was 320 eV, and the Fermi level was smeared by 0.2 eV [51]. Brillouin zone integration was performed on a $25 \times 25 \times 1$ k-point mesh for surface unit cell and proportionally smaller meshes for larger supercells.

2.4. Electrochemical characterization

Electrochemical measurements were performed via cyclic voltammetry (CV) using a Solartron Analytical instrument (AMETEK model 1470E). The half-cell system consisted of a pre-treated glassy carbon working electrode (0.196 cm^2), a platinum-wire counter electrode, and a reference electrode. Catalyst inks were prepared as follows: the Pd/GNS and Pd_3Y/GNS catalysts were suspended in a solution of de-ionized water, isopropyl alcohol, and Nafion® ionomer solution (5 wt.%) and sonicated for 30 min. The working electrode was fabricated using the thin-film electrode method [52]. Electrodes were prepared as previously described [53]. For the Pd/GNS and Pd_3Y/GNS catalysts, the metal loading on a glassy carbon electrode (5 mm diameter) was 40 $\mu g\,cm^{-2}$. The ORR polarization curves for the RDE in an O_2-saturated 0.1 M NaOH or 0.1 M $HClO_4$ solution at room temperature were obtained at a sweep rate of 10 $mV\,s^{-1}$ through a positive sweep at rotation rates of 400, 900, 1600 and 2500 rpm. To experiment the ethanol oxidation, a solution of 1 M ethanol (C_2H_6OH) in 1 M KOH was employed as the electrolyte solution and electrochemical measurements were performed after degassing with nitrogen of ultra-high purity. The CV curves of these catalysts were recorded in each electrolyte solution at a sweep rate of 50 $mV\,s^{-1}$. Potentials were determined using a Hg/HgO/OH^- (MMO) electrode for 0.1 M NaOH electrolyte and double-junction Ag/AgCl/3 M KCl reference electrode for 0.1 M $HClO_4$ electrolyte. All potentials were referenced to the reversible hydrogen electrode (RHE).

3. Results and discussion

3.1. Structural properties of Pd/GNS and Pd_3Y/GNS

The chemically synthesized GNSs, which possess sufficient surface areas to accommodate highly concentrated Pd and Pd_3Y nanoparticle catalysts, exhibit a sheet-like morphology, as shown in Fig. 1. In general, particle size is likely larger with higher metal loadings on supports, which results in a smaller active surface area for the case of carbon black—a widely used support material [54,55]. Therefore, high metal dispersions are difficult to obtain with a carbon support, especially with a high metal loading, because the metals tend to sinter due to weak interactions between the metal and the carbon [54,55]. Fig. 1a–c demonstrates that the uniformly dispersed Pd and Pd_3Y nanoparticles (with diameters less than 4 nm) were successfully deposited on the GNS at loadings up to 60 wt.%. The morphology, average particle size, and particle size distribution of the prepared materials, observed from the TEM images, are shown in Fig. 1 and summarized in Table 1. More than 150 different particles that were visible on the micrographs were employed to estimate the average particle size. For GNS-supported Pd and Pd_3Y, as shown in Fig. 1, uniform and finely dispersed nanoparticles were observed on the GNS support, even with high metal loadings of 60 wt.%. The sizes of the highly dispersed nanoparticle of

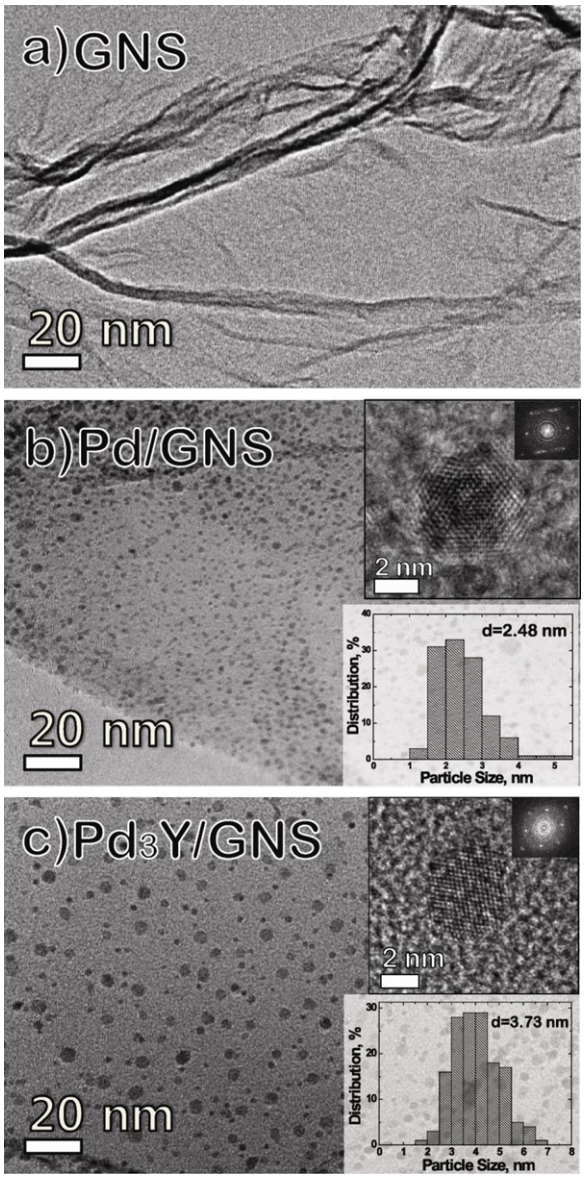

Fig. 1. TEM images of (a) GNS, and GNS-supported (b) Pd and (c) Pd_3Y with corresponding histograms of particle sizes. Insets (b) and (c) show the high-magnification TEM micrograph along with a microdiffraction pattern from particles of Pd and Pd_3Y.

the GNS-supported Pd and Pd_3Y were estimated to be ca. 2.48 and 3.73 nm, respectively (see Table 1). The high-magnification TEM micrographs along with a micro-diffraction pattern were added in the inset of the Fig. 1. The dominant features are consistent with the crystalline face centered cubic (FCC) structure indicated in the relevant digital diffractogram. A lower magnification image of the particles dispersed on the graphene substrate shows the coexistence of large as well as small sized particles as shown histogram of Fig. 1b and c, where the particles represent both types of the tetrahedron and truncated octahedron structures. It is known there is a kinetically controlled shape transformations from tetrahedron-to-octahedron-to-cubic [56]. The distance between the nearest neighbored atoms of Pd_3Y particles was increased compared with that of Pd particles, indicating the Pd_3Y alloy.

Fig. 2 shows XRD patterns of the GNS-supported Pd and Pd_3Y catalysts, in which the characteristic peaks of a crystalline face centered cubic (FCC) Pd phase from (1 1 1), (2 0 0), (2 2 0), and (3 1 1) planes appeared at the corresponding diffraction angles. There were no noticeable peaks for a pure Y or its oxides in our XRD

Table 1
Structural and physicochemical parameters of the GNS-supported Pd and PdY catalysts using XRD, TEM, and XPS analyses.

Samples	Heat treatment temp. (°C)	2θmax[a] (°)	Lattice parameter[b] (Å)	TEM particle size[c] (nm)	XPS[d]		Pd/Y[e] (atomic ratio)
					Pd $3d_{5/2}$ core level BE (eV)	Pd $3d_{3/2}$ core level BE (eV)	
60 wt.% Pd/GNS	250	68.20	3.886	2.48 ± 0.69	335.55	340.81	–
64 wt.% Pd_3Y/GNS	250	67.47	3.923	3.73 ± 1.12	335.44	340.70	2.6

[a] The angular position of Pd (2 2 0) reflection peak.
[b] Lattice parameter calculated from XRD measurement.
[c] Mean particle diameter of the sample from TEM image using at least 150 visible particles.
[d] Binding energy of Pd $3d_{5/2}$ and Pd $3d_{3/2}$ corrected from XPS analysis.
[e] Surface Pd/Y atomic ratio calculated from XPS by using peak area normalized on the basis of sensitivity factors.

measurements, indicating a good degree of alloying between Pd and Y. In particular, the diffraction peaks were shifted to lower 2θ values in the Pd_3Y/GNS catalysts by adding Y content, as described in the right inset figure for the enlarged Pd (2 2 0) peak; such shift could be an evidence for the alloy formation between Pd and Y. The lattice parameters for the Pd/GNS and Pd_3Y/GNS were evaluated using the angular position ($2\theta_{max}$) of the (2 2 0) peak [57] from Fig. 2. The lattice parameter changes of the Pd/GNS and Pd_3Y/GNS catalysts are also given in Table 1. While the lattice parameter of 3.886 Å for the Pd/GNS catalyst is in a good agreement with that of nanosized Pd particle reported in elsewhere [58–61], the crystalline lattice parameters for the Pd_3Y/GNS catalysts are greater than that of Pd/GNS catalyst and appear to increase with addition of Y elements, indicating the lattice dilation as Y atoms are incorporated to the FCC lattice of Pd crystallites

3.2. Surface state analysis for Pd/GNS and Pd_3Y/GNS

XPS analyses were used to elucidate the electronic structures and composition of the prepared Pd and Pd_3Y nanoparticles on the GNS supports. The core-level shift measured using XPS is a good indicator of the center of the occupied d-states [28,29,57,62]. In the d-band center model, the electronic structure of the surface metal and its catalytic activity is correlated [30]. This model has been used to explain why the alteration of electronic structures can significantly change catalytic properties [14,18,30]. The binding energy (BE) of the major spin–orbit split doublet (Pd $3d_{5/2}$ and Pd $3d_{3/2}$) for Pd/GNS (Fig. 3) appeared at approximately 335.55 and 340.81 eV, respectively, and were attributed to the presence of metallic Pd (Pd^0) [29,43,63]. Another doublet, with the BEs for the Pd $3d_{5/2}$ and $3d_{3/2}$ peaks at approximately 337.1 and 342.36 eV, respectively, was attributed to a higher oxidation state similar to that of PdO [29,63]. The Pd $3d_{5/2}$ core-level BEs of GNS-supported Pd and Pd_3Y were estimated to be at 335.55 and 335.44 eV, respectively (see Table 1). The core-level BEs of Y $3d_{5/2}$ appear at around 156.13 and 156.96 eV indicating the metallic and higher oxidation states similar to that of Y oxide, respectively. The peak positions of the zero-valent Pd (Pd^0) were shifted because d–d band hybridization occurs between Pd and the second metal [28,29]. It is noteworthy that the BE shift to lower energies appears in the Pd_3Y/GNS catalyst compared to the Pd/GNS catalyst, which may be caused by electronegativity differences, leading to charge transfer from the less electronegative Y to the more-electronegative Pd. To investigate a composition of Pd and Y atoms, the surface Pd/Y atomic ratio evaluates to 2.6, calculated from the XPS data by using peak areas normalized on the basis of sensitivity factors (see Table 1). Table 1 summarizes structural and physicochemical parameters of the GNS-supported Pd and Pd_3Y catalysts prepared in this study through particle size, lattice parameter, binding energy and surface composition analysis from TEM, XPS and XRD. It appears that the Pd and Pd_3Y nanoparticles are well synthesized on GNS with reliable chemical composition through the impregnation method.

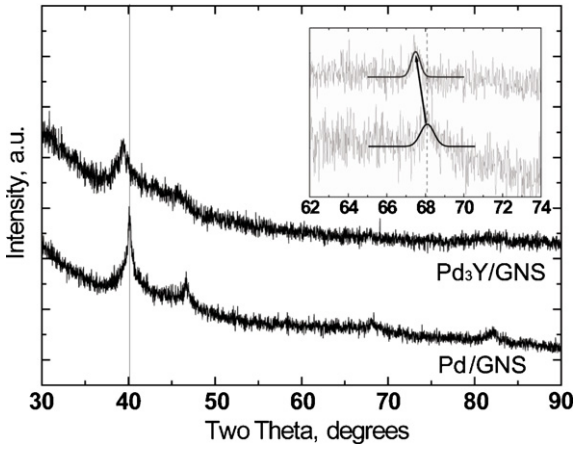

Fig. 2. XRD patterns of the GNS-supported Pd and Pd_3Y.

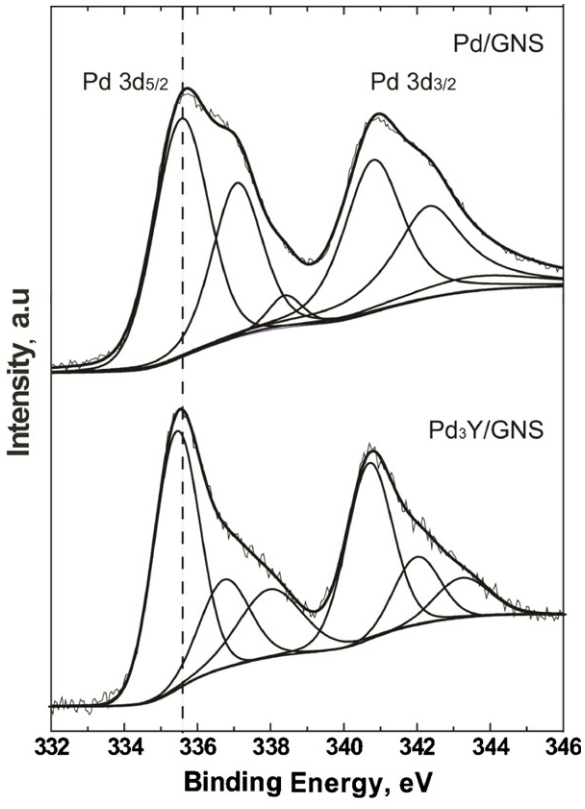

Fig. 3. XPS Pd 3d core-level spectra of the GNS-supported Pd and Pd_3Y.

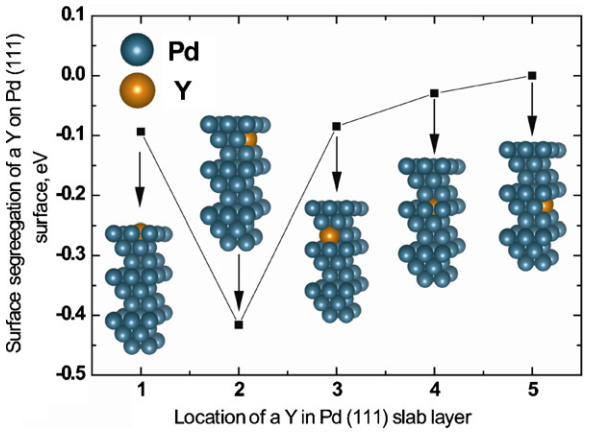

Fig. 4. The surface segregation energies of a nine-layer (2 × 2) Pd slab with one Pd atom replaced by a Y atom. The energy is set to zero when Y is brought from the center of the slab in 5th layer from the surface.

3.3. First principle DFT calculations

Prior to investigation of the electronic structure of Pd and Pd_3Y alloy, we calculated the segregation energy of Y to design optimized structure of Pd_3Y alloy. Fig. 4 shows the first-principles DFT calculated segregation energies of a Y atom in a nine-layer of (2 × 2) Pd slab. The energy is set to zero when Y is brought from the center of the slab (the 5th layer from the surface). Our calculation indicates that Y atom prefers to stay at the 2nd layer of Pd slab (just below the top surface). In general, a solute metal having a low surface energy moves to surface of a host metal and is likely segregated [33,64–66]. The atomic size of Pd and Y are about 1.37 Å and 1.82 Å, and the surface energies are 2.050 J m^{-2} and 1.125 J m^{-2}, respectively, as previously reported [67]. Thus, we designed the 3 types of models, which were Pd (1 1 1), homogeneous Pd_3Y (1 1 1) and Pd_3Y^* (1 1 1) with 50% Y in the 2nd layer near the surface as shown in Fig. 5. Fig. 6 shows density of state spectra and optimized structures of Pd (1 1 1), Pd_3Y (1 1 1) and Pd_3Y^* (1 1 1) after *ab initio* DFT calculations. The Pd d-band center position calculated from the spectra is used as a descriptor of surface reactivity for ORR and EOR. The occupied d-band electron numbers are estimated ca. 8.82, 8.95, and 9.09 for Pd (1 1 1), Pd_3Y (1 1 1) and Pd_3Y^* (1 1 1), respectively. The electron occupation of the d band of Pd on Pd_3Y (1 1 1) and Pd_3Y^* (1 1 1) increases compared with that on Pd (1 1 1). It is because electronegativity differences could lead to charge transfer from the less electronegative Y to the more-electronegative Pd. The d-band center position of the alloy surfaces is quite different from that of corresponding pure Pd (1 1 1), accompanied by hybridization of the d-band by Y atoms. The d-band center position of Pd (1 1 1) is evaluated at the −1.83 eV (related to Fermi level) and it is good agreement with previous reports [18,68]. In Fig. 6, theoretical d-band center of homogeneous Pd_3Y (1 1 1), found to be −1.90 eV, is negatively shifted than Pd (1 1 1) in our calculation. On the other hand, d-band center position of each Pd atom numbered to #3 and #4 on the surface in Fig. 6d shifts toward the Fermi level compared with Pd (1 1 1) in the model of Pd_3Y^* having 50% Y in 2nd layer, while atom numbered to #5 shifts downward the Fermi level. That is, this conflict could be comprehensive due to distribution of Y atoms on the near surface and site dependency of atom on surface. In general, a negative core level shift is interpreted by electron filling of the atom, e.g., the electron transfer from Y to Pd. Thus, the lower BEs shift of Pd_3Y nanoparticles measured from XPS and the occupied d-band electron numbers calculated by the first principles computation is well consistent with the previous studies [25,57]. Greeley et al. has also calculated the O adsorption energy for both 25% and 50% 2nd metal concentration in the 2nd layer for several systems designed, and they referred whether the 2nd metal concentration in the sublayer is stoichiometric or higher depending on the system and the method by which it is formed [33,34,69]. Hence, structure of prepared Pd_3Y nanoparticles in this work implies that Y preferred to occupy in the inner layer than the outlayer. The density of state (DOS) of prepared catalysts at the Fermi level plays an important role on the chemisorption bond of the adsorbates and significantly influences the electrocatalytic activity. For the Pd_3Y/GNS catalysts, therefore, the closer the position of d-band center position toward the Fermi level could predict the stronger the interactions with adsorbents (e.g., oxygen).

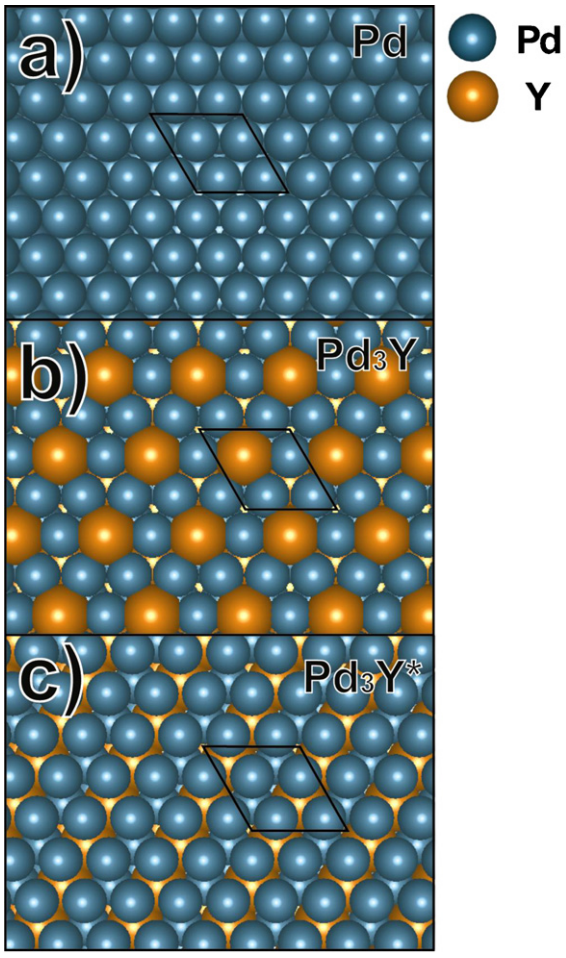

Fig. 5. Top view of initial slab model for the unit cells on the (1 1 1) surface of (a) Pd, (b) Pd_3Y and (c) Pd_3Y^* with 50% Y in the 2nd layer.

3.4. Oxygen reduction reaction (ORR) studies of Pd/GNS and Pd_3X/GNS

Fig. 7 showed typical CVs of the Pd catalysts in a 0.1 M NaOH electrolyte at room temperature, which were obtained using a half-cell system at a scan rate of 50 mV s^{-1} in the potential range of 0–1.4 V vs. RHE. The electrochemical active surface (EAS) value of Pd/GNS and Pd_3Y/GNS was evaluated in a 0.1 M NaOH solution by assuming that the monolayer PdO reduction charge is 405 μC cm^{-2} on Pd surface. The value was accompanied by the electrochemical reduction of a close packed monolayer of PdO, because Pd exhibits a poor definition of the hydrogen adsorption/desorption region [61,70]. The fully activated EAS values calculated from PdO reduction charge were 46.3 and 30.9 m^2 g^{-1} for Pd/GNS and Pd_3Y/GNS, respectively. The values are compatible with other reports which were investigated at highly concentrated nanoparticles on GNS [61,70].

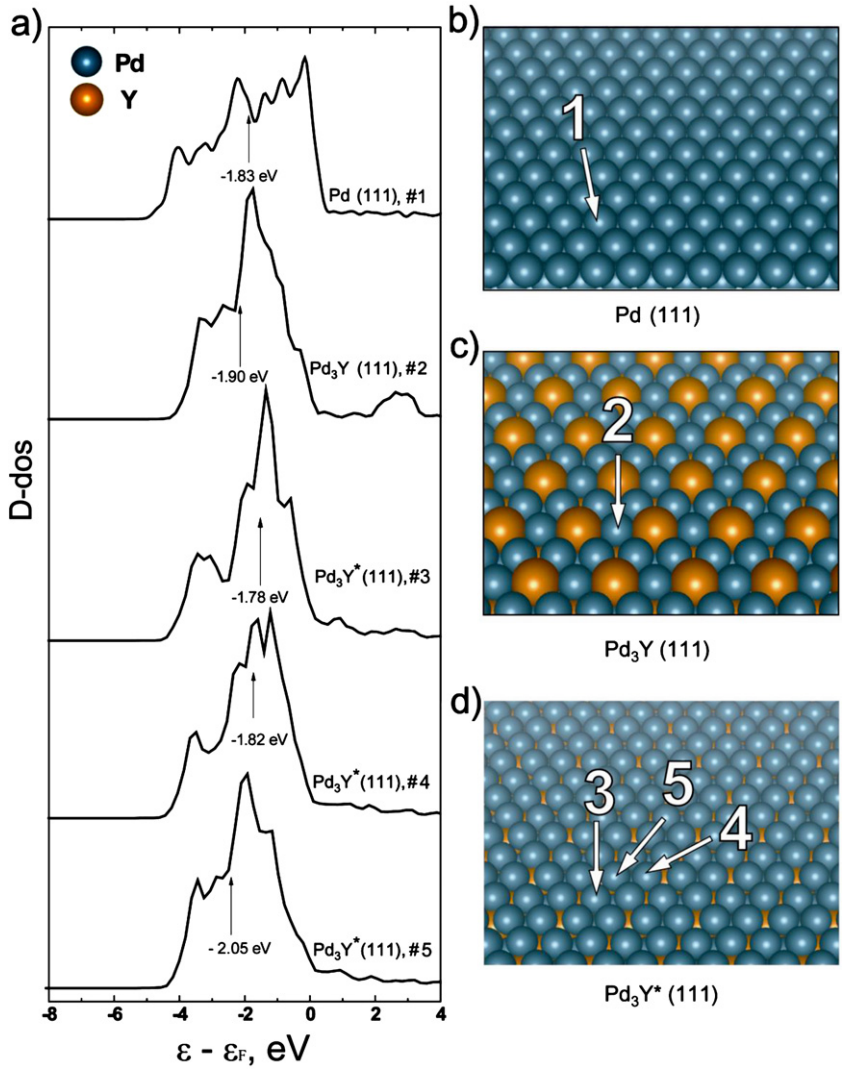

Fig. 6. (a) D-dos spectra and d-band centers (ε_d) with respect to the Fermi level (ε_F), calculated for each numbered atom pointed on Pd (1 1 1), Pd_3Y (1 1 1) and Pd_3Y^* (1 1 1) in (b–d).

The rotating-disk electrode (RDE) technique has been conventionally used to investigate the kinetics of reactions while maintaining steady-state conditions for the ORR [71–73]. The GNS-supported Pd and Pd_3Y catalysts were investigated for the ORR activity. The polarization curves for the RDEs both in 0.1 M NaOH and 0.1 M $HClO_4$ saturated with O_2 gas at 298 K were obtained using a sweep rate of 10 mV s^{-1} in the range from 1.2 to 0.1 V vs. RHE. The experimental values for the limited diffusion current density (j_d) at the given rotation rates were plotted. The ORR polarization curves of the catalysts were obtained at rotation rates of 400–2500 rpm in O_2-saturated 0.1 M NaOH and 0.1 M $HClO_4$ solutions. The ORR-limited current increases with the rotation rate, and is proportional to the square root of the rotation rate. The plots in Fig. 8 are known as Levich–Koutecky plots [53,74] and are based on the following equation:

$$j_d = 0.62 n_e F D^{2/3} \nu^{-1/6} c_0 \omega^{1/2} = B c_0 \omega^{1/2} \quad (1)$$

where n_e is the number of electrons transferred per O_2 molecule; F is the Faraday constant; D is the diffusion coefficient of dissolved O_2 in solution; ν is the kinematic viscosity of the solution; ω is the rotation rate; and c_0 is the concentration of dissolved O_2 in solution. The electrochemical reduction of O_2 is a multi-electron transfer reaction with two main possible pathways: one involves the transfer of two electrons to produce H_2O_2, and the other involves a direct four-electron pathway to produce water and hydroxide in acidic and alkaline media, as described by the following equation [75]:

$$O_2 + 2H_2O + 4e^- \rightarrow 4OH^- \quad \text{(alkaline media)} \quad (2)$$

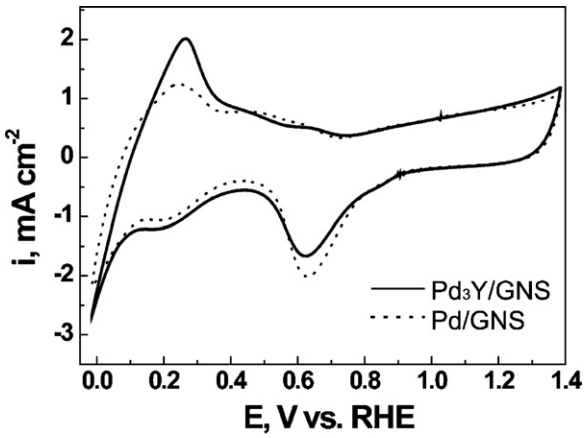

Fig. 7. Cyclic voltammograms of the GNS-supported Pd and Pd_3Y catalysts in a 0.1 M NaOH electrolyte at a 50 mV s^{-1} scan rate at room temperature. Current densities were normalized to the geometric area of the working electrode (ca. 0.196 cm^2).

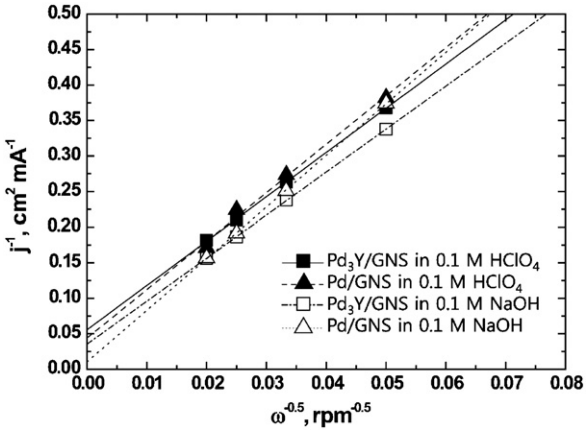

Fig. 8. Levich–Koutecky plots of GNS-supported Pd and Pd_3Y for the ORR measured from RDE in O_2-saturated 0.1 M $HClO_4$ and 0.1 M NaOH solutions.

$$O_2 + 4H^+ + 4e^- \rightarrow 2H_2O \quad \text{(acidic media)} \tag{3}$$

From the Levich–Koutecky plots in this work, the n_e for the ORR on Pd/GNS and Pd_3Y/GNS catalysts were calculated to be approximately 4 with water and hydroxide in acidic and alkaline solutions saturated with O_2 (see Table 2).

Fig. 9 shows the oxygen-reduction current densities for the positive sweep on Pd/GNS and Pd_3Y/GNS at a single rotation rate (1600 rpm) in O_2-saturated 0.1 M NaOH and 0.1 M $HClO_4$ solutions.

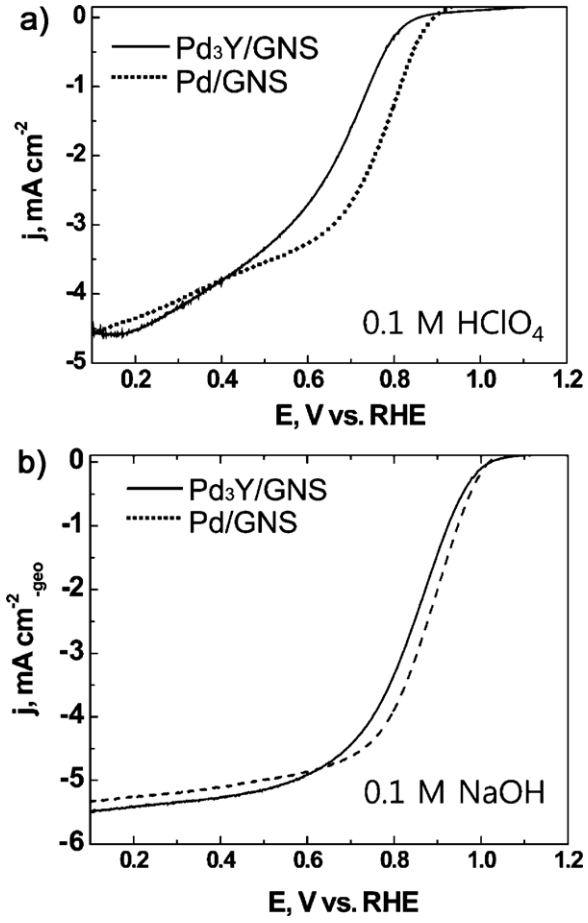

Fig. 9. Comparison of the polarization curves of GNS-supported Pd and Pd_3Y for the ORR in O_2-saturated (a) 0.1 M $HClO_4$ and (b) 0.1 M NaOH solutions with a sweep rate of 10 mV s^{-1} at room temperature; rotation speed: 1600 rpm.

Relative to RHE, the ORR on the catalysts occurs at more positive potentials under alkaline conditions than under acidic conditions, as previously reported [61,76]. The kinetic currents, with respect to the activation and diffusion, are calculated by the following equation [71]:

$$\frac{1}{j} = \frac{1}{j_k} + \frac{1}{j_d} + \frac{1}{j_f} = \frac{1}{j_k} + \frac{1}{BC_o\omega^{1/2}} + \frac{1}{nFc_fD_f} \tag{4}$$

where j is the current measured at the mixed diffusion-kinetics control region from the ORR polarization curve; j_k is the kinetic current calculated from Eq. (4); j_d is the boundary-layer diffusion-limited current; B is the Levich constant; and j_f is the limiting diffusion current controlled by reactant diffusion in the film. D_f and C_f represent the diffusion coefficient and the solubility of the reactant in the Nafion film, respectively. The j_k estimated for GNS-supported Pd and Pd_3Y in acidic and alkaline conditions are summarized in Table 2. For the Pd/GNS and Pd_3Y/GNS, the kinetic current density, j_k, at a potential of 0.85 V vs. RHE were 0.093 and 0.001 mA cm^{-2} in acidic media, and 1.50 and 0.89 mA cm^{-2} in alkaline media, respectively. The j_k of Pd_3Y/GNS was lower than that of the Pd/GNG under both of alkaline and acidic condition. From the XPS results in Fig. 3 and Table 1, the Pd $3d_{5/2}$ core levels for Pd_3Y/GNS were shifted to a lower BE with respect to Pd/GNS, which indicates a upshift of the d-band center. The high-lying d-band center of Pd in a Pd alloy should exhibit slower kinetics than Pd, which suggests that a strong Pd—O bond was formed [18]. The results are in good agreement with previous reports, in which the d-bands of Pd were elucidated using the d-band center model [14,28,30,34].

3.5. Ethanol oxidation reaction (EOR) studies of the Pd/GNS and Pd_3Y/GNS

The Pd is generally known as one of the good catalysts for ethanol electrooxidation under alkaline condition even compared with Pt [77–79]. The oxidation of ethanol involves 12 electrons as following reaction:

$$C_2H_5OH + 3H_20 \rightarrow 2CO_2 + 12H^+ + 12e^- \tag{5}$$

However, the main product of the EOR on Pd surface is not CO_2 but acetate ions because the Pd has a limited capacity for C—C bond cleavage. Therefore, it has been proposed that ethanol oxidation is determined by the degree of CH_3CO_{ads} and OH_{ads} coverage [26,80] as following mechanism [25,26,80,81]:

$$Pd + OH^- \leftrightarrow Pd + OH_{ads} + e^- \tag{6}$$

$$Pd + CH_3CH_2OH \leftrightarrow Pd\text{-}(CH_3CH_2OH)_{ads} \tag{7}$$

$$Pd\text{-}(CH_3CH_2OH)_{ads} + 3OH^- \rightarrow Pd\text{-}(CH_3CO)_{ads} + 3H_2O + 3e^- \tag{8}$$

$$Pd\text{-}(CH_3CO)_{ads} + Pd\text{-}3OH_{ads} \rightarrow Pd\text{-}CH_3COOH + Pd \tag{9}$$

$$Pd\text{-}CH_3COOH + OH^- \rightarrow Pd + CH_3COO^- + H_2O \tag{11}$$

It has been suggested that the rate determining step is Eq. (9) [25,80]. Accordingly, the OH_{ads} adsorbed on the electrode is important for EOR because the adsorbed reaction intermediate species of ethanol is removed by adsorbed hydroxyl ions and release free active catalytic sites.

To elucidate promoting effects of Y in Pd catalysts, the catalytic activity of the Pd/GNS and Pd_3Y/GNS catalysts was examined using the CV technique for the ethanol electrooxidation reactions. The scan potential was from −0.0 to 1.3 V (vs. RHE) at a 50 mV s^{-1} scan rate. In general, as shown in Fig. 10, the shapes of the CV curves represent the typical ethanol electrooxidation reactions and indicate two anodic current peaks in the positive and negative sweeps. The forward anodic peak current density (j_f) is attributed to the EOR during the positive sweep. The reverse anodic peak current density

Table 2
Electrochemical parameters of the Pd/GNS and Pd_3Y/GNS catalysts characterized by electrochemical analyses.

Catalysts	Real active surface area (cm^2)[a]	Active surface area ($m^2\ g^{-1}$)[a]	ORR				EOR		
			Kinetic current density @ 0.85 vs. RHE, j_k ($mA\ cm^{-2}$)[b]		Number of electrons transferred, n_e		Forward peak current density, j_f		j_f/j_b[e]
			Acid	Alkaline	Acid	Alkaline	j_m ($mA\ mg^{-1}_{-Pd}$)[c]	j_{real} ($mA\ cm^{-2}$)[d]	
60 wt.% Pd/GNS	3.63	46.3	0.093	1.50	3.89	4	1325	1.47	0.94
64 wt.% Pd_3Y/GNS	2.43	30.9	0.001	0.89	3.86	3.96	1780	2.95	1.18

[a] Using the monolayer PdO reduction charge of 405 $\mu C\ cm^{-2}$.
[b] Kinetic current density normalized from geometric surface area, 0.196 cm^{-2}.
[c] Forward anodic peak current density normalized by Pd mass at 50 $mV\ s^{-2}$.
[d] Forward anodic peak current density normalized to the real Pd surface area.
[e] Ratio of forward (j_f) to reverse (j_b) peak current density.

(j_b) is due to the oxidation of the incompletely oxidized carbonaceous residues on the catalyst surface in the negative sweep. Likely, the latter intermediates are strongly adsorbed on the Pd surface, which blocks the active catalyst sites for the next turnover, thus rendering the anodic reactions more sluggish. As summarized in Table 2, the current densities were normalized by the active surface area of the electrode; the Pd mass and real Pd surface area were compared. By comparing the characteristics of the CVs in Fig. 10, the addition of Y to Pd substantially enhanced the catalytic activity for ethanol electrooxidation. For the Pd/GNS and Pd_3Y/GNS, the real active area-normalized current densities, j_{real}, at approximately 0.9 V during the positive sweep were 1.47 and 3.95 $mA\ cm^{-2}$, respectively. The Pd_3Y/GNS showed at least 100% higher activity in the electrooxidation of ethanol than Pd/GNS. Also, the Pd mass -normalized current, j_m, demonstrated that the activity of Pd_3Y/GNS (1780 $mA\ mg^{-1}_{-Pd}$) is approximately 34% higher than that of Pd/GNS (1325 $mA\ mg^{-1}_{-Pd}$).

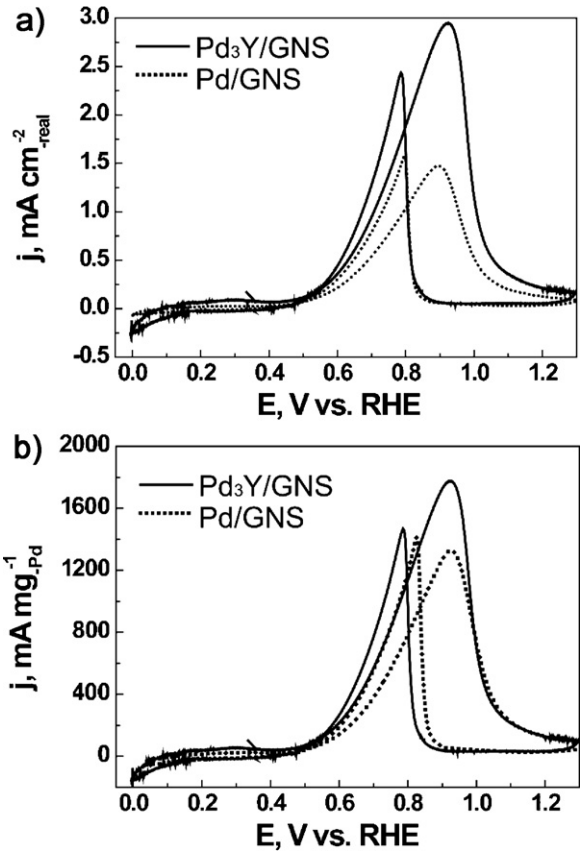

Fig. 10. (a) Cyclic voltammetry of the GNS-supported Pd and Pd_3Y catalysts in 1 M KOH with 1 M ethanol (C_2H_5OH) at a 50 $mV\ s^{-1}$ scan rate at room temperature. (b) Comparison of current densities after normalization to the Pd mass and the real Pd surface area for the prepared catalysts.

These results are consistent with the previous studies that the lower BEs shift measured from XPS enhances the catalytic activity for EOR [25,57,82]. With respect to electronic change, the XPS data in Fig. 3 and Table 1 demonstrated that higher d-band center position increases the bond energy between Pd and OH^-, compared with the Pd/GNS catalyst. This phenomenon represents that OH^- ions are more easily adsorbed onto Pd_3Y/GNS than Pd/GNS. The OH_{ads} adsorbed on the electrode will oxidize the residual intermediates (e.g., CH_3CO_{ads}, CH_3COOH) if the interaction of OH^- on Pd surface is strong [26]. This could help to remove more intermediates and release more active sites on the surface of the catalyst. The oxidative removal of intermediate species could be inferred from the peak current intensity ratio between the forward peak current, j_f, and the backward peak current, j_b, in which the latter is generally recognized as the current produced during the electrooxidation of residual intermediate species on the Pd surface after ethanol electrooxidation. As shown in Fig. 10 and Table 2, the j_f/j_b ratios were 0.94 for the Pd/GNS, but increased in the presence of Y to 1.18 for the Pd_3Y/GNS catalysts. Thus, these features imply that electrode kinetics using the Pd_3Y/GNS yield the efficient electrooxidation of ethanol with the small activation barrier.

4. Conclusion

This work studied a fundamental relationship on Pd and Pd_3Y nanoparticles between the experimentally or theoretically determined surface electronic structure (the d-band center position) and activity for the ORR and EOR. The uniformly dispersed Pd and Pd_3Y nanoparticles (with diameters less than 4 nm), which were prepared via the impregnation method coupled with a subsequent heat treatment under hydrogen gas, were successfully deposited on the GNS at loadings up to 60 wt.% for the ORR and EOR activities. The Pd $3d_{5/2}$ core levels for Pd_3Y/GNS were observed to shift to a lower BE with respect to Pd/GNS, indicating an upshift of d-band center. From *ab initio* DFT calculation, theoretical d-band center positions of surface atoms for Pd_3Y (1 1 1) and Pd_3Y^* (1 1 1) having 50% Y in 2nd layer are negatively or positively shifted than that of Pd (1 1 1) because it is depend on the site on surface and the distribution of Y atoms on the near surface. Based on the computational results, it implies that Y prefers to occupy the site just below the top surface. The activity of the highly concentrated Pd electrocatalysts on GNSs is higher than the Pd_3Y nanoparticles on GNS for ORR under both acidic and alkaline conditions because of strong interaction between Pd and O. For the EOR, however, the activity of Pd_3Y/GNS is much higher than that of Pd/GNS under alkaline condition. The

d-band center model well supported these results for ORR and EOR activity. The modified electronic structure of the Pd by Y might influence the binding energy of oxygen species on the Pd surface and therefore, change the electrocatalytic activity for the ORR and EOR. These results suggest that GNS-supported Pd based alloy catalysts, controlling the electronic structure of Pd by 2nd metal, could be considered a good electrocatalyst materials via for use in both acidic and alkaline fuel cell.

Acknowledgements

This work was supported by the New & Renewable Energy R&D program (no. 20103020030020 and 20113020030020) under the Korea Government Ministry of Knowledge Economy, and funded by National Research Foundation of Korea (no. 20120005212) and the Global Frontier R&D Program on Center for Multiscale Energy System (0420-20110157) by Korea Government. It was also supported by DGIST R&D Program of the Ministry of Education, Science and Technology of Korea (12-BD-0405) and by the KISTI with supercomputing resources including technical support (KSC-2012-C2-15).

References

[1] W. Vielstich, A. Lamm, H.A. Gasteiger, Handbook of Fuel Cells Fundamentals Technology and Applications, John Wiley & Sons Ltd., London, 2003.
[2] H.A. Gasteiger, J.E. Panels, S.G. Yan, Journal of Power Sources 127 (2004) 162–171.
[3] S.M. Choi, M.H. Seo, H.J. Kim, W.B. Kim, Carbon 49 (2011) 904–909.
[4] K.C. Neyerlin, W. Gu, J. Jorne, H.A. Gasteiger, Journal of the Electrochemical Society 154 (2007) B631–B635.
[5] S.M. Choi, M.H. Seo, H.J. Kim, E.J. Lim, W.B. Kim, International Journal of Hydrogen Energy 35 (2010) 6853–6862.
[6] M.H. Seo, S.M. Choi, H.J. Kim, J.H. Kim, B.K. Cho, W.B. Kim, Journal of Power Sources 179 (2008) 81–86.
[7] M.H. Seo, S.M. Choi, H.J. Kim, W.B. Kim, Electrochemistry Communications 13 (2011) 182–185.
[8] M.H. Seo, E.J. Lim, S.M. Choi, H.J. Kim, W.B. Kim, Topics in Catalysis 53 (2010) 678–685.
[9] N.P. Subramanian, X. Li, V. Nallathambi, S.P. Kumaraguru, H. Colon-Mercado, G. Wu, J.-W. Lee, B.N. Popov, Journal of Power Sources 188 (2009) 38–44.
[10] R. Bashyam, P. Zelenay, Nature 443 (2006) 63–66.
[11] J.S. Spendelow, A. Wieckowski, Physical Chemistry Chemical Physics 9 (2007) 2654–2675.
[12] J.S. Park, S.H. Park, S.D. Yim, Y.G. Yoon, W.Y. Lee, C.S. Kim, Journal of Power Sources 178 (2008) 620–626.
[13] K. Asazawa, K. Yamada, H. Tanaka, A. Oka, M. Taniguchi, T. Kobayashi, Angewandte Chemie 119 (2007) 8170–8173.
[14] M.H. Shao, P. Liu, J. Zhang, R.R. Adzic, Journal of Physical Chemistry B 111 (2007) 6772–6775.
[15] M. Pourbaix, Atlas of Electrochemical Equilibria in Aqueous Solutions, Pergamon Press Ltd., Headington Hill Hall, Oxford, 1974.
[16] Y.-C. Wei, C.-W. Liu, Y.-W. Chang, C.-M. Lai, P.-Y. Lim, L.-D. Tsai, K.-W. Wang, International Journal of Hydrogen Energy 35 (2010) 1864–1871.
[17] M.H. Shao, K. Sasaki, R.R. Adzic, Journal of the American Chemical Society 128 (2006) 3526–3527.
[18] M.H. Shao, T. Huang, P. Liu, J. Zhang, K. Sasaki, M.B. Vukmirovic, R.R. Adzic, Langmuir 22 (2006) 10409–10415.
[19] S. Zhang, X. Yuan, H. Wang, W. Meĭrida, H. Zhuc, J. Shen, S. Wu, J. Zhang, International Journal of Hydrogen Energy 34 (2009) 388–404.
[20] E. Antolini, J.R.C. Salgado, M.J. Giz, E.R. Gonzalez, International Journal of Hydrogen Energy 30 (2005) 1213–1220.
[21] E. Antolini, E.R. Gonzalez, Journal of Power Sources 195 (2010) 3431–3450.
[22] L. Jiang, A. Hsu, D. Chu, R. Chen, Journal of the Electrochemical Society 156 (2009) B370–B376.
[23] L. Jiang, A. Hsu, D. Chu, R. Chen, Electrochimica Acta 55 (2010) 4506–4511.
[24] C. Bianchini, P.K. Shen, Chemical Reviews 109 (2009) 4183–4206.
[25] S.T. Nguyen, H.M. Law, H.T. Nguyen, N. Kristian, S. Wang, S.H. Chan, X. Wanga, Applied Catalysis B: Environmental 91 (2009) 507–515.
[26] Z.X. Liang, T.S. Zhao, J.B. Xu, L.D. Zhu, Electrochimica Acta 54 (2009) 2203–2208.
[27] U.B. Demirci, Journal of Power Sources 173 (2007) 11–18.
[28] M. Wakisaka, S. Mitsui, Y. Hirose, K. Kawashima, H. Uchida, M. Watanabe, Journal of Physical Chemistry B 110 (2006) 23489–23496.
[29] K. Lee, O. Savadogo, A. Ishihara, S. Mitsushima, N. Kamiya, K.I. Otac, Journal of the Electrochemical Society 153 (2006) A20–A24.
[30] B. Hammer, J.K. Norskov, Nature 376 (1995) 238–240.
[31] B. Hammer, J.K. Norskov, Surface Science 343 (1995) 211–220.
[32] M. Shao, K. Sasaki, N.S. Marinkovic, L. Zhang, R.R. Adzic, Electrochemistry Communications 9 (2007) 2848–2853.
[33] J. Greeley, M. Mavrikakis, Nature Materials 3 (2004) 810–815.
[34] J. Greeley, I.E.L. Stephens, A.S. Bondarenko, T.P. Johansson, H.A. Hansen, T.F. Jaramillo, J. Rossmeisl, I. Chorkendorff, J.K. Nørskov, Nature Chemistry 1 (2009) 552–556.
[35] V.R. Stamenkovic, B. Fowler, B.S. Mun, G. Wang, P.N. Ross, C.A. Lucas, N.M. Markovic, Science 315 (2007) 493–497.
[36] H. Liu, C. Song, L. Zhang, J. Zhang, H. Wang, D.P. Wilkinson, Journal of Power Sources 155 (2006) 95–110.
[37] A. Peigney, C. Laurent, E. Flahaut, R.R. Bacsa, A. Rousset, Carbon 39 (2001) 507–514.
[38] K.S. Novoselov, A.K. Geim, S.V. Morozov, D. Jiang, M.I. Katsnelson, I.V. Grigorieva, S.V. Dubonos, A.A. Firsov, Nature 438 (2005) 197–200.
[39] A.K. Geim, K.S. Novoselov, Nature Materials (2007) 183–191.
[40] K.I. Bolotin, K.J. Sikes, Z. Jiang, M. Klima, G. Fudenberg, J. Hone, P. Kim, H.L. Stormer, Solid State Communications 146 (2008) 351–355.
[41] C. Soldano, A. Mahmood, E. Dujardin, Carbon 48 (2010) 2127–2150.
[42] K. Gotoh, K. Kawabata, E. Fujii, K. Morishige, T. Kinumoto, Y. Miyazaki, H. Ishida, Carbon 47 (2009) 2112–2142.
[43] S.M. Choi, M.H. Seo, H.J. Kim, W.B. Kim, Synthetic Metals 161 (2011) 2405–2411.
[44] N.I. Kovtyukhova, P.J. Ollivier, B.R. Martin, T.E. Mallouk, S.A. Chizhik, E.V. Buzaneva, A.D. Gorchinskiy, Chemistry of Materials 11 (1999) 771–778.
[45] P. Hohenberg, W. Kohn, Physical Review 136 (1964) B864–B871.
[46] W. Kohn, L.J. Sham, Physical Review A 140 (1965) A1133–A1138.
[47] G. Kresse, J. Furthmüller, Physical Review B 54 (1996) 11169.
[48] G. Kresse, D. Joubert, Physical Review B 59 (1999) 1758.
[49] P.E. Blöchl, Physical Review B 50 (1994) 17953.
[50] J.P. Perdew, K. Burke, M. Ernzerhof, Physical Review Letters 77 (1996) 3865.
[51] M.P.A.T. Methfessel, Physical Review B 40 (1989) 3616–3621.
[52] T.J. Schmidt, H.A. Gasteiger, G.D. Stab, P.M. Urban, D.M. Kolb, R.J. Behm, Journal of the Electrochemical Society 145 (1998) 2354–2358.
[53] K.J.J. Mayrhofer, D. Strmcnik, B.B. Blizanac, V. Stamenkovic, M. Arenz, N.M. Markovic, Electrochimica Acta 53 (2008) 3181–3188.
[54] J. Perez, E.R. Gonzalez, E.A. Ticianelli, Electrochimica Acta 44 (1998) 1329–1339.
[55] L. Genies, R. Faure, R. Durand, Electrochimica Acta 44 (1998) 1317–1327.
[56] Z.L. Wang, Journal of Physical Chemistry B 104 (2000) 1153–1175.
[57] J.H. Kim, S.M. Choi, S.H. Nam, M.H. Seo, S.H. Choi, W.B. Kim, Applied Catalysis B: Environmental 82 (2008) 89–102.
[58] R. Lamber, S. Wetjen, N.I. Jaeger, Physical Review B 51 (1995) 10968–10971.
[59] J. Xu, L. Ouyang, G.-J. Da, Q.-Q. Song, X.-J. Yang, Y.-F. Han, Journal of Catalysis 285 (2012) 74–82.
[60] L. Zhang, K. Lee, J. Zhang, Electrochimica Acta 52 (2007) 3088.
[61] L. Jiang, A. Hsu, D. Chu, R. Chen, Journal of the Electrochemical Society 156 (2009) B643–B649.
[62] H.J. Kim, Y.S. Kim, M.H. Seo, S.M. Choi, W.B. Kim, Electrochemistry Communications 11 (2009) 446–449.
[63] I.G. Casella, M. Contursi, Journal of Electroanalytical Chemistry 588 (2006) 147–154.
[64] D. Tománek, A.A. Aligia, C.A. Balseiro, Physical Review B 32 (1985) 5051–5056.
[65] B.C. Han, A.V. d. Ven, G. Ceder, B.-J. Hwang, Physical Review B 72 (2005) 205409.
[66] A.V. Ruban, H.L. Skriver, J.K. Norskov, Physical Review B 59 (1999) 15990–16000.
[67] L. Vitos, A.V. Ruban, H.L. Skriver, J. Kollár, Surface Science 411 (1998) 186–202.
[68] F.H.B. Lima, J. Zhang, M.H. Shao, K. Sasaki, M.B. Vukmirovic, E.A. Ticianelli, R.R. Adzic, Journal of Physical Chemistry C 111 (2007) 404–410.
[69] K.A. Kuttiyiel, K. Sasaki, Y. Choi, D. Su, P. Liu, R.R. Adzic, Energy & Environmental Science 5 (2012) 5297.
[70] T. Chierchie, C. Mayer, W.J. Lorenz, Journal of Electroanalytical Chemistry 135 (1982) 211–220.
[71] N.M. Markovic, B.N. Grgur, P.N. Ross, Journal of Physical Chemistry B 101 (1997) 5405–5413.
[72] S.J. Yoo, H.Y. Park, T.Y. Jeon, I.S. Park, Y.H. Cho, Y.E. Sung, Angewandte Chemie International Edition 47 (2008) 9307–9310.
[73] H.A. Gasteiger, N.M. Markovic, P.N. Ross Jr., J. Phys. Chem. 99 (1995) 8290–8301.
[74] U.A. Paulus, T.J. Schmidt, H.A. Gasteiger, R.J. Behm, Journal of Electroanalytical Chemistry 495 (2001) 134–145.
[75] J. Guo, A. Hsu, D. Chu, R. Chen, Journal of Physical Chemistry C 114 (2010) 4324–4330.
[76] W.E. Mustain, K. Kepler, J. Prakash, Electrochemistry Communications 8 (2006) 406–410.
[77] C. Xu, P.k. Shen, Y. Liu, Journal of Power Sources 164 (2007) 527–531.
[78] H.T. Zheng, S. Chen, P.K. Shen, Electrochemistry Communications 9 (2007) 1563–1566.
[79] H.T. Zheng, Y. Li, S. Chena, P.K. Shen, Journal of Power Sources 163 (2006) 371–375.
[80] J. Liu, J. Ye, C. Xu, S.P. Jiang, Y. Tong, Electrochemistry Communications 9 (2007) 2334–2339.
[81] Z. Zhang, L. Xin, K. Sun, W. Li, International Journal of Hydrogen Energy 36 (2011) 12686–12697.
[82] S.W. Lee, S. Chen, W. Sheng, N. Yabuuchi, Y.-T. Kim, T. Mitani, E. Vescovo, Y. Shao-Horn, Journal of the American Chemical Society (2009) 15669–15677.